



Full Length Article

Charging process simulation of a coil by a self-regulating high- T_c superconducting flux pump

Pengbo Zhou ^{a,b,*}, Yanyu Zhou ^a, Mark Ainslie ^c, Asef Ghabeli ^b, Francesco Grilli ^b, Guangtong Ma ^a^a State Key Laboratory of Rail Transit Vehicle System, Southwest Jiaotong University, Chengdu 610000, China^b Institute for Technical Physics, Karlsruhe Institute of Technology, Karlsruhe 76344, Germany^c Department of Engineering, King's College London, London WC2R 2LS, UK

ARTICLE INFO

Keywords:

Numerical simulation
Electrical circuit model
High-temperature superconductor (HTS)
Flux pumps
H-formulation
HTS coils
HTS modeling

ABSTRACT

Self-regulating high-temperature superconducting (HTS) flux pumps enable direct current injection into a closed-loop superconducting coil without any electrical contact. In this work, the process of charging a coil by a self-regulating HTS flux pump is examined in detail by numerical modeling. The proposed model combines an **H**-formulation finite element method (FEM) model with an electrical circuit, enabling a comprehensive evaluation of the overall performance of self-regulating HTS flux pumps while accurately capturing local effects. The results indicate that the proposed model can capture all the critical features of a self-regulating HTS flux pump, including superconducting properties and the impact of the secondary resistance. When the numerical results are compared to the experimental data, the presented model is found to be acceptable both qualitatively and quantitatively. Based on this model, we have demonstrated how the addition of a milliohm range, normal-conducting secondary resistance in series with the charging loop can improve the charging process. In addition, its impact on the charging performance is revealed, including the maximum achievable current, charging speed, and the generated losses. The modeling approach employed in this study can be generalized to the optimization and design of various types of flux pumps, potentially expediting their practical application.

1. Introduction

High-temperature superconducting (HTS) coils constructed by HTS wires are ideal for generating strong magnetic fields due to their current-carrying capability and superior in-field performance. Due to the rapid advancement of commercially available High-Temperature Superconducting (HTS) wires, HTS coils are now showing great promise for practical implementation in various applications. Their application include high-field magnets [30,34,41,35], magnetic levitation [22,21,20], wind turbines [25,43,23], and motors/generators [36]. In conventional setups, a power supply is constantly connected to keep the current flowing within the HTS coils, and the current is transmitted through a pair of thick current leads that connect the cryogenic and ambient environments. This results in heat losses that can severely limit the performance and efficiency of HTS applications.

Flux pumps have been vigorously investigated to address this issue. Flux pumps are devices that can inject direct current into a closed-loop superconducting coil without any electrical contact [24]. Flux pumps are preferred over conventional power supply methods for energizing high-temperature superconducting (HTS) coils [5,42,40]. The princi-

ple behind the HTS flux pump involves exploiting the non-linear electromagnetic characteristics of HTS materials to produce a rectifying effect. [15,3,31,32]. Typically, the rectifying effect in HTS tape is achieved by exposing its surface to a powerful magnetic field [17,19,8,11]. However, achieving such a field strength can be challenging if the field magnet is placed outside the cryostat. Thus, the field magnet must be placed inside the cryostat, leading to an additional heat load on the cooling system. To address this issue, researchers have made significant efforts, such as adding an iron yoke and a ferromagnetic slice beneath the HTS stator [4,38,39,29]. A self-regulating HTS flux pump is superior to other types of flux pumps, because it requires fewer heat-dissipating elements in the cryogenic environment [12,48,46]. The input alternating current can be converted to direct current for the coil connected to the HTS bridge by partially driving it above the critical current via a current adjustment in the HTS bridge. The output current of self-regulating HTS flux pumps has been increased to several thousand amperes [10], confirming the enormous potential of this technology. To characterize and optimize the performance of self-regulating flux pumps, for increased

* Corresponding author at: State Key Laboratory of Traction Power, Southwest Jiaotong University, Chengdu 613100, China.

E-mail addresses: pengbo.zhou@kit.edu (P. Zhou), 2491068471@qq.com (Y. Zhou), mark.ainslie@kcl.ac.uk (M. Ainslie), asef.ghabeli@kit.edu (A. Ghabeli), francesco.grilli@kit.edu (F. Grilli), gma@swjtu.edu.cn (G. Ma).

practical applications, a fast and accurate numerical simulation of their electromagnetic behavior is required.

Various numerical models have been developed in recent years, which can be divided into two main categories. The first category is based on the finite-element method (FEM). The model proposed by [13] is the first FEM model for evaluating the performance of transformer-rectifier-type HTS flux pumps. Later, [48] employed a similar approach for modeling a self-regulating HTS flux pump. However, the basic operating principle is only qualitatively reproduced in such models with a number of simplifications and is unable to capture all the crucial features, especially the impact of secondary resistance. The secondary resistance, which is commonly used in flux pumps, is achieved by using a copper sheet with resistance in the milliohm ($m\Omega$) range. Therefore, the secondary resistance, in this case, is several orders of magnitude greater than the resistance of the soldered joints, which typically exhibit resistances in the tens of nanohms ($n\Omega$) range. It has been experimentally proved that the secondary resistance has a tremendous impact on the charging performance of transformer-rectifier-type HTS flux pumps [27,6]. The second category of models is based on lumped-parameter circuit models [28,45,26]. Although this approach can simulate the overall charging process, the limited understanding of the specific local physical characteristics of the HTS material poses a challenge for utilizing these models in a comprehensive system design and optimization. In this study, we present a modeling approach that combines an H-formulation FEM model with an electrical circuit. Although the formulations used may differ, the fundamental concept of this modeling strategy is consistent with existing literature on this subject [47,7,9,33]. This integrated approach enables accurate simulation of the dynamic charging process of a coil utilizing a self-regulating flux pump. The proposed model incorporates the superconducting effect and provides a comprehensive understanding of the entire system. Moreover, it enables the investigation of the effect of secondary resistance on key parameters such as maximum load saturation current and charging rate. This research provides valuable insights into the potential mechanisms by which secondary resistance can enhance excitation performance, and the losses that occur in different components of the system are quantified.

The article is structured as follows: Section 2 provides a brief overview of the configuration and operating principle of a self-regulating HTS flux pump from a circuit perspective. Section 3 describes the proposed modeling approach. In Section 4, we present the experimental setup used to validate the model. Section 5 presents a detailed analysis of the charging process of a coil and the characteristics of the overall system. Finally, Section 6 provides concluding remarks.

2. Problem configuration

The self-regulating HTS flux pump circuit is similar to a conventional rectifier. The difference is that the whole circuit, including the load and the rectifier, is a superconductor. Consequently, during their “on-state,” they exhibit complete superconductivity and can operate in a quasi-persistent current mode. Fig. 1 demonstrates the equivalent circuit diagram of a self-regulating HTS flux pump. It consists of two primary components: a charging loop and a load loop, which are formed by three elements connecting the loops together: i) a superconducting magnetic coupler, ii) a rectifying HTS bridge, and iii) a load HTS coil. The bifilar structure shown in Fig. 1 is preferred for constructing the HTS bridge due to its ability to eliminate the inductive voltage component [18], which is responsible for undesirable current ripples during the charging process [16]. Additionally, as emphasized by [27,6], the secondary resistance R_s connected to the charging loop is crucial for achieving the maximum current through the coil by resisting the increase of the charging loop direct component, and thus strengthening the load current. Interested readers are referred to [12]

for a better understanding of the fundamental physics underlying the self-regulating HTS flux pump.

From a circuit perspective, the operational process is as follows [48]. By applying an alternating magnetic flux Φ to the circuit through the primary winding of the magnetic coupler, a large alternating current i_c is induced in the charging loop. At the beginning of the process, the HTS bridge shorts the load HTS coil, preventing any current from flowing through the coil. By controlling the waveform of the bridge current i_b , so that its positive peak value exceeds the HTS bridge critical current while the rest of the portion is below the critical value, the resistance of the HTS bridge R_b varies periodically due to the non-linear electromagnetic properties of the superconductor. During each positive period, a net voltage V_L is generated across the HTS bridge due to the switching effect of the HTS bridge, and the load HTS coil L , which is connected to the HTS bridge, gradually charges. As the load current i_L increases, the bridge current i_b , which is a combination of the secondary and load current, biases to the negative direction, causing the net voltage V_L to decrease. The charging process is complete when the net value of V_L drops to zero. After that, by removing the source of magnetic flux, the load current i_L can circulate and be maintained for an extended period in the superconducting load loop formed by the coil and the bridge. Additionally, the magnetic flux can be reapplied to compensate for any decay in the load current caused by joint resistance or an external magnetic field.

3. Model description

To characterize this flux pump, a 2D FEM model coupled with a circuit model is established. Specifically, the charging loop, including the superconducting magnetic coupler and the HTS bridge is modeled by a 2D FEM model. On the other hand, the load loop is simulated with the circuit model, in which the load HTS coil is assumed to be an ideal coil consisting of an inductance and a resistance without considering its critical current or any dynamic effects arising from screening current.

The structure of the 2D FEM model is shown in Fig. 2. An asymmetrical alternating current is supplied to the primary winding to generate the magnetic field, which has an asymmetric triangular waveform with a higher positive peak value than its negative peak value, and the ratio between them is $N:1$ ($N > 1$). To avoid the direct current component, the positive period of the asymmetric triangular waveform is N times longer than the negative period, and the ratio of positive to negative peak values is inversely proportional to the ratio of their respective peak durations. The charging loop of the flux pump is formed by the parallel superconducting (SC) tapes #1 and #2, with SC tape #1 serving as the secondary winding and SC tape #2 serving as the HTS bridge. A closed iron core passes through the primary winding and the charging loop, enhancing the magnetic coupling between them. Normally, the current-carrying capacity of the secondary winding exceeds the magnitude of the induced current circulating within it, resulting in the entire current flowing through the superconducting layer. Therefore, in order to model SC tape #1, only the superconducting layer is considered, while other metal layers such as substrate, copper stabilizer, and silver layer are ignored. Since the transport current passing through the HTS bridge (SC tape #2) exceeds its critical current during each period, the generated resistance could be comparable to that of other metal layers. Therefore, the current sharing effect between the SC tape layers cannot be ignored. Generally, most of the current would migrate into the copper stabilizers due to their large cross-section and low resistivity [50]. Therefore, as shown in Fig. 3, the geometry employed for simulating the HTS bridge is a superconducting layer sandwiched between two copper stabilizers.

The model is implemented using the **H**-formulation [37,1], which is derived from Maxwell's equations:

$$\nabla \times \mathbf{E} + \frac{\partial \mathbf{B}}{\partial t} = \nabla \times (\rho \nabla \times \mathbf{H}) + \mu_0 \mu_r \frac{\partial \mathbf{H}}{\partial t} = 0, \quad (1)$$

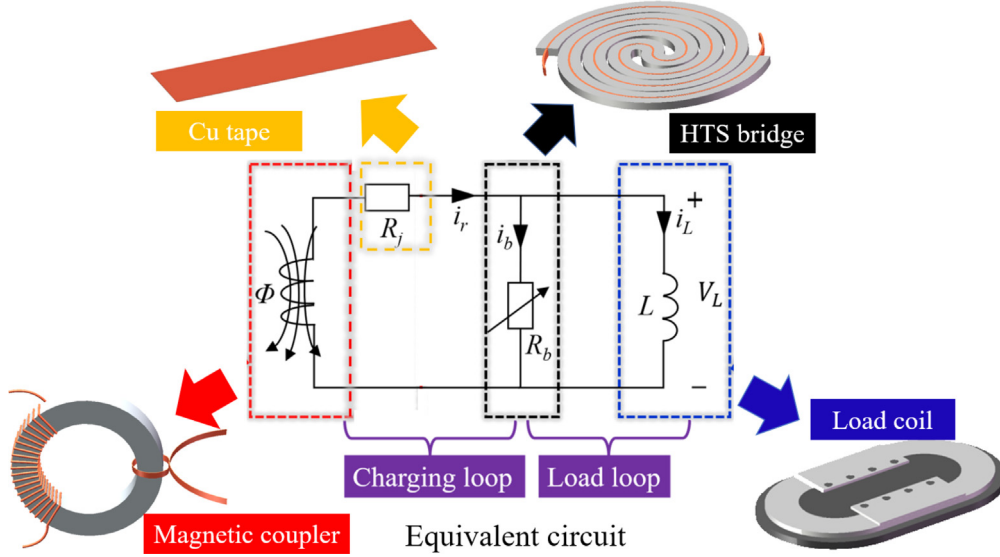


Fig. 1. Diagram of the self-regulating HTS flux pump circuit model and the load HTS coil being charged. All paths of the equivalent circuit are made of HTS wire, except for R_j which is made of copper.

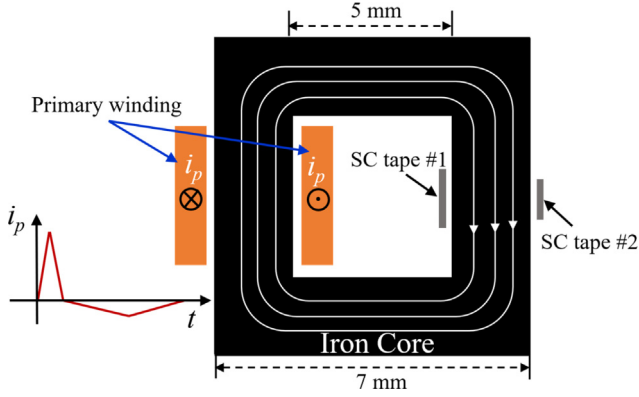


Fig. 2. Diagram of the 2D FEM model for the self-regulating HTS flux pump. The waveform of the current injected into the primary winding is also shown on the left.



Fig. 3. Schematic of the modeled HTS bridge (SC tape #2) cross-section (not to scale).

$$\nabla \times \mathbf{H} = \mathbf{J}, \quad (2)$$

where μ_0 denotes the permeability of free space, μ_r denotes the relative magnetic permeability of the material, and ρ denotes the resistivity of the material. Since the 2D model has translational symmetry, the current density vector \mathbf{J} can be represented as $[0, 0, J_z]$, implying that the current only flows in the z-direction. The magnetic field vector and electric field vector can be represented as $[H_x, H_y, 0]$ and $[0, 0, E_z]$, respectively. Typically, the model can be effectively simulated by solv-

ing the above equations. However, this model is not sufficient for incorporating the secondary resistance into the charging loop, which is crucial for improving the charging performance of the flux pump. The main issue is that the model representing the cross-section of superconducting tapes, which assumes infinitely long conductors, ignores end effects such as series-connected resistances. Therefore, an extra electric field component has been added in the governing equation for SC tape #1 for simulating the effect of the secondary resistance R_j , which differs from the conventional \mathbf{H} -formulation [44]. Along the secondary winding, namely, SC tape #1, the contributions superconducting tapes and from the secondary resistances can be separately accounted for in the computation of the electric field:

$$\mathbf{E} = \mathbf{E}_{sc} + \mathbf{E}_j, \quad (3)$$

where \mathbf{E}_{sc} is the contribution to the electric field solely by the superconductor and \mathbf{E}_j is electric field generated by the secondary resistances. For the low-frequency regime (below kHz) investigated in this study, the distribution of the electric field in normal conductors is nearly uniform in the low-frequency regime (below kHz) investigated here, therefore:

$$\mathbf{E}_j = \bar{R}_j i. \quad (4)$$

$$\bar{R}_j = \frac{R_j}{l}. \quad (5)$$

Here, \bar{R}_j is the secondary resistance per unit length, and i is the current flowing through it, and l is the length of the charging circuit in the model. Substituting Eq. (4) into Eq. (1), the governing equation for SC tape #1 becomes:

$$\mu_0 \mu_r \frac{\partial \mathbf{H}}{\partial t} + \nabla \times (\rho \nabla \times \mathbf{H} + \bar{R}_j i) = 0. \quad (6)$$

The resistivity of the superconductor is modeled using an E - J power law, which describes the dependence of resistivity on the electric field in the material, combined with a Kim-like model that takes into account the magnetic field dependence of the critical current:

$$\rho_{sc} = \frac{E_c}{J_c(\mathbf{B})} \left| \frac{\mathbf{J}}{J_c(\mathbf{B})} \right|^{n-1}, \quad (7)$$

$$J_c(\mathbf{B}) = \frac{J_{c0}}{(1 + \sqrt{k^2 B_{\parallel}^2 + B_{\perp}^2 / B_0})^\alpha}, \quad (8)$$

where E_c is the characteristic electric field for the critical current ($1 \mu\text{V}/\text{cm}$), $n = 28$ is the power-law exponent, B_{\parallel} and B_{\perp} represent the magnetic flux density components that are parallel and perpendicular, to the broad surface of the tape, respectively, and B_0, k , and α are material-related parameters with values of 0.0425, 0.29515 and 0.7, respectively [49]. J_{c0} is the critical current density derived from the self-field critical current. The self-field critical current of the SC tape #1 is assumed to be 255 A at 77 K to ensure that its current-carrying capability is higher than the induced current passing through it, while the self-field critical current of SC tape #2 is assumed to be 108 A at 77 K. The resistivity of the copper stabilizers is assumed to be 1.97 nΩm and resistivity for the rest of the domains is assumed to be 1 Ωm. The relative permeability is assumed to be $\mu_r = 1000$ for the iron core and 1 for all the other materials. The HTS coil is simulated by a lumped parameter element with an inductance $L = 210 \mu\text{H}$ and a joint resistance $R_L = 100 \text{ n}\Omega$. These values are derived from the experimental values presented by [6,48]. The relevant simulation parameters are listed in Table 1. The voltage induced in the load HTS coil can be calculated by integrating the electric field over the cross-section of SC tape #2:

$$V_L(t) = \frac{\int_S E_z(t) ds}{S} l_b, \quad (9)$$

where S is the cross-sectional area of the HTS bridge, and l_b is the length of the HTS bridge, which is assumed to be of unit length in this study. The voltage is connected to COMSOL's Electrical Circuit interface, which is comprised of the voltage source connected in series with both the inductance and resistance [16]. With a global constraint, the resulting current i_{am} is unidirectionally coupled back to the FEM model,

$$-i_r + i_b + i_L = \int_{s_1} \mathbf{J} ds + \int_{s_2} \mathbf{J} ds + i_L$$

where s_1 and s_2 denote the cross-sections of SC tapes #1 and #2, respectively. An ammeter is used for measuring the current flowing through the coil i_L . This global constraint ensures that the sum of currents flowing through the secondary winding, bridge, and load connected to the circuit is equal to zero.

4. Experiment set-up

To further validate the effectiveness of the proposed model, we compare the measured bridge voltage previously reported in experiments by [6] with the corresponding values calculated by our model. The experimental set-up is shown in Fig. 4 consists of four main components: 1) a power source (PBZ20-20) capable of generating asymmetrical voltage/current; 2) a superconducting transformer having a 20-turn copper primary winding and a single-turn superconducting secondary winding. A 6 mm wide secondary superconducting tape obtained from SuperPower is used to construct the superconducting winding, with a superconducting layer thickness of $1 \mu\text{m}$. This tape has a critical current I_c of 255 A; 3) A 4 mm wide SuperPower tape with a superconducting layer thickness of 1 m and an I_c of 100 A

Table 1
Values of the parameters used in the simulation.

Component	Parameter	Value
Air	Resistivity	$1 \Omega \cdot \text{m}$
	Magnetic permeability	$4\pi \times 10^{-7} \text{ H/m}$
Secondary coil	Width	6 mm
	Critical current	255 A
	Magnetic permeability	$4\pi \times 10^{-7} \text{ H/m}$
Bridge	Width	4 mm
	Critical current	108 A
	Length	1 m
Load circuit	Resistance	$1 \times 10^{-7} \Omega$
	Inductance	$210 \mu\text{m}$

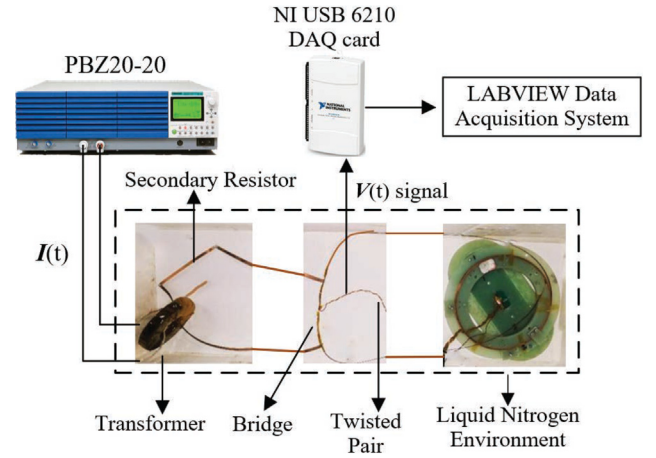


Fig. 4. Experimental set-up of a self-regulating HTS flux pump.

was used for the superconducting bridge; 4) a 20-turn circular HTS coil with a self-inductance of $210 \mu\text{H}$ serves as the load. A summary of the relevant parameters is provided in Table 2. A piece of copper wire is used to introduce secondary resistance into the charging loop. Using this a method, the value of the secondary resistance can be adjusted by using different lengths of copper wires. To measure the resistive component of the bridge voltage, a twisted pair of voltage taps is employed, which is attached close along the center line of the HTS bridge, to eliminate the inductive voltage [14,2]. The measured signal is acquired with a sampling resolution of $96 \mu\text{V}$ using an NI USB 6210 DAQ card.

5. Results and discussion

5.1. Characterization of charging performance

First, we investigate the charging performance under an applied frequency of 50 Hz. The secondary resistance is assumed to be $1.2 \text{ m}\Omega$ [6]. The waveform of the current i_p that is injected into the primary winding is shown in Fig. 5. The ratio between the positive and negative peak values is set to 4:1 with a peak positive value of 200 A and a peak negative value of 50 A, and the ratio between the positive and negative periods is set to 1:4 (see Section 3).

The detailed waveform of both the load current i_L and the bridge current i_b are presented in Fig. 6. The waveform of the bridge current is identical to the primary current, whereas the load current exhibits a distinct ladder shape. The load current begins to ramp up when the bridge current surpasses the dynamic critical current of the bridge. This critical current is obtained by integrating the critical current density $J_c(\mathbf{B})$ over the superconducting region of the bridge. The load current remains constant for the remaining part of the period. This result

Table 2
Parameters of the experimental set-up

Component	Parameter	Value
Primary coil	Number of turns	20
	Width	6 mm
Secondary coil	Number of turns	1
	Width	6 mm
	Critical current	255 A
Bridge	Width	4 mm
	Critical current	100 A
	Length	10 cm
Load coil	Number of turns	20
	Voltage criterion E_{c0}	10^{-4} V/m
	Self-field critical current	97.5 A
	Self-inductance	$210 \mu\text{H}$

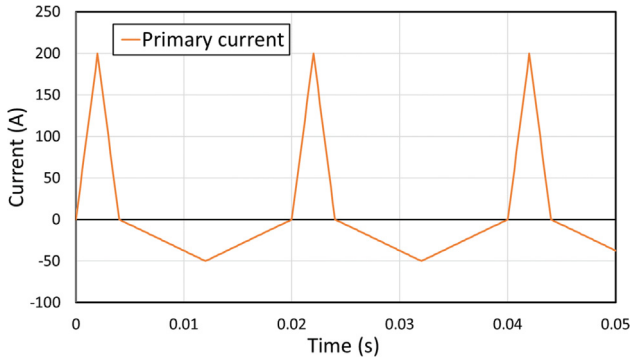


Fig. 5. Waveform of the simulated primary current i_p for an applied frequency of 50 Hz.

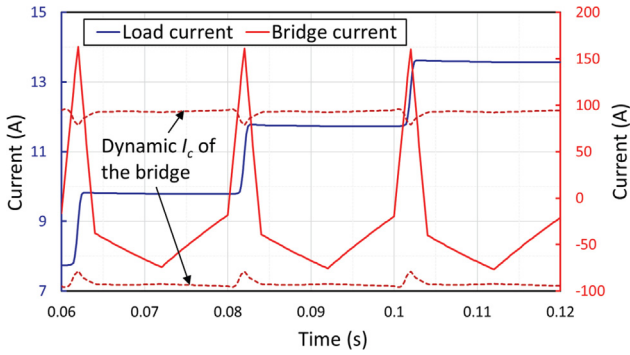


Fig. 6. Detailed simulated waveforms of load current and bridge current for an applied frequency of 50 Hz and secondary resistance of 1.2 mΩ.

is qualitatively consistent with the measurement reported by [12], validating our modeling strategy.

Fig. 7 shows the load current accumulated over 200 cycles, which presents a trend similar to that of a first-order circuit. Since the joint resistance (100 nΩ) connected in series is almost negligible, the cause of this phenomenon is the reduction of the voltage applied to the coil. As the load current i_L increases, the bridge current i_b (the detailed waveform of it is shown in Fig. 6) gradually shifts in the opposite direction, as illustrated in Fig. 8. As depicted in Fig. 9 (a), the induced voltage V_L is decreased, resulting in a reduction of the current increment during each period of the charging process because the integration of load voltage is reduced. As a consequence, the charging speed is reduced. For better characterization, the net values of the bridge current and the voltage, which is also the load voltage, are also shown in

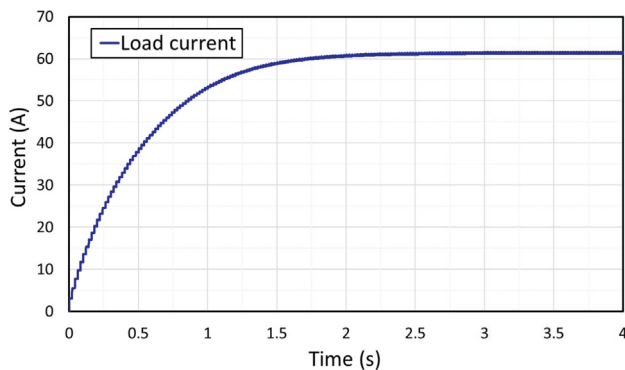


Fig. 7. Waveform of the simulated load current for an applied frequency of 50 Hz and secondary resistance of 1.2 mΩ.

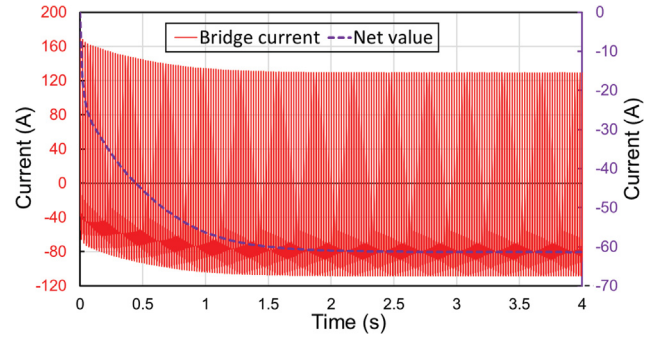


Fig. 8. Simulated bridge current and its net value for an applied frequency of 50 Hz and secondary resistance of 1.2 mΩ.

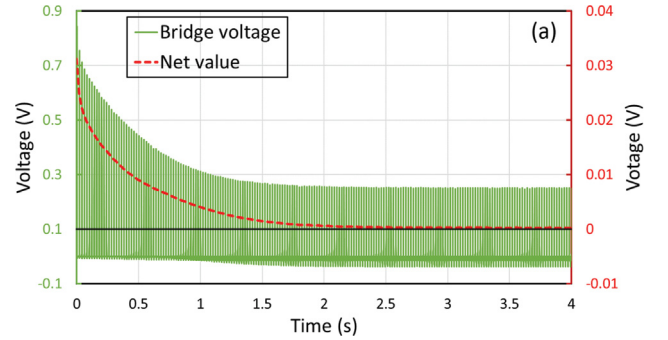


Fig. 9. Simulated bridge voltage (also the load voltage) and its net value for an applied frequency of 50 Hz and secondary resistance of 1.2 mΩ.

Figs. 8 and 8, respectively. It is clear that the charging process ends when the net value of the bridge voltage reaches zero. Concurrently, the load current approaches a saturation level, which is equivalent to the current drop within the bridge. The net values are obtained by

$$I = \frac{1}{T} \int_t^{t+T} i_b dt, \quad (11)$$

$$V = \frac{1}{T} \int_t^{t+T} V_L dt, \quad (12)$$

where T is the period. The above analysis numerically demonstrates, the entire charging process described in Section 3.

As presented in Fig. 8, the magnitude of the current through the HTS bridge is much higher than its critical current (108 A), especially during the initial stages of the charging process, where the peak value can reach twice as high as the critical value. In reality, under such a high transport current, the superconductor will be driven from its superconducting state to a flux flow state or a normal state. The resulting voltage drastically varies within one period. To further verify the effectiveness of this model, we compared the simulated bridge voltage with the experimental data. We implemented the experimental setup used by [6] in Section 4. The main difference between the simulation and the experiment is that the length of the HTS bridge used in the experiment is one-tenth of the length used in the simulation. Therefore, for a more accurate comparison, the measured voltage has been multiplied by 10.

Figs. 10 (b)-(g) show the simulated and measured HTS bridge voltages at three different stages: at the beginning, as the load current increases, and when the current saturates. The simulation has successfully replicated the experimental results. Aside from the basic feature that the positive voltage decreases and the negative voltage becomes noticeable during the charging process, the simulation also reproduces the negative peak that occurs when the positive value drops to zero. To

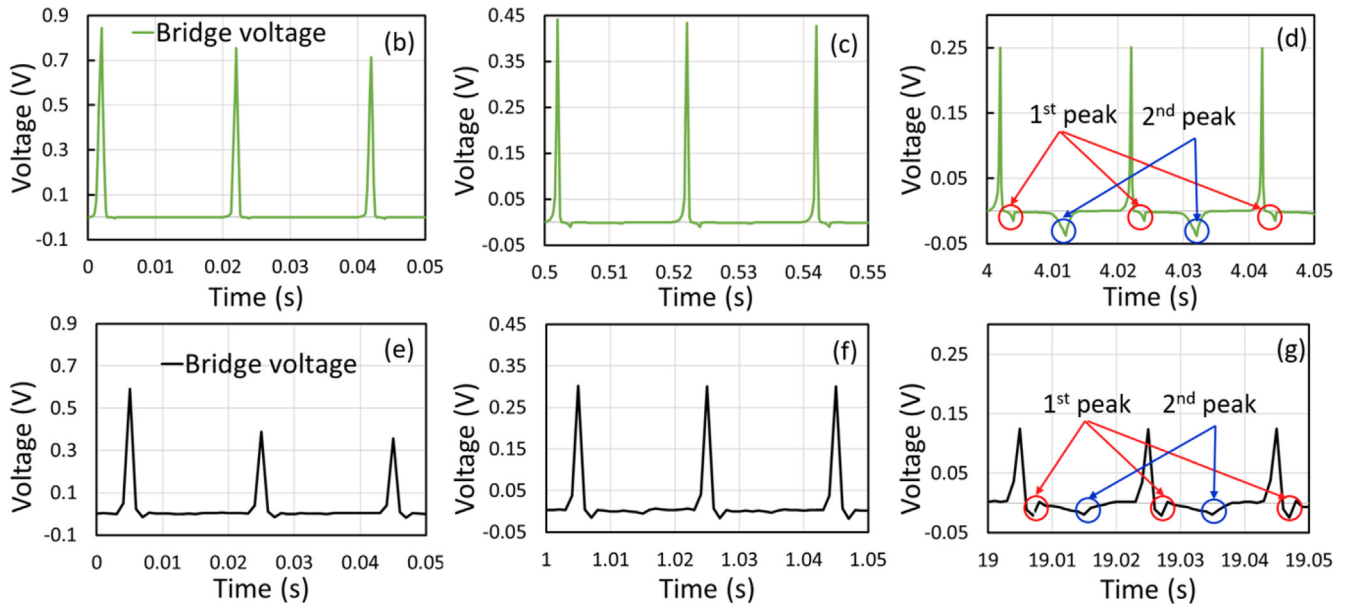


Fig. 10. Bridge voltage at different charging stages: (b)-(d) simulation results, (e)-(g) experimental results.

be more specific, there are two negative peaks existing in the bridge voltage waveform. The first peak is attributed to the hysteretic behavior of the superconductor, and the second peak is due to the fact that the negative current surpasses the critical current of the bridge. Additionally, the amplitude of the simulated bridge voltage without considering any thermal factors is not lower, but rather higher than the measured results. A possible reason for this phenomenon is that the HTS bridge is deployed far away from other magnetic field sources in the experiment, whereas in the simulation, the HTS bridge is located close to the iron core. The magnetization of the iron core amplifies the local magnetic field in the HTS bridge, resulting in a lower critical current and, consequently, a higher induced voltage. This effect can be reproduced in the model by adding another circuit to connect the secondary winding and the HTS bridge and implementing the HTS bridge in a separate FEM model. Nevertheless, based on the validation of the experiment, we can conclude that the proposed model produces acceptable results both qualitatively and quantitatively.

To clarify the behavior of the bridge voltage, Fig. 11 demonstrate the separation of the bridge current, which is only possible through simulation. The current flowing through the HTS bridge can be categorized into two parts: the superconducting (SC) current and the copper (Cu) current. Despite the continuous drop in the bridge current in the negative direction, the SC current remains relatively constant in each positive period, while the Cu current decreases over time. Furthermore, the current that the superconducting layer can carry is about 1.3 times higher than its critical current. In this region, the superconductor is in its flux flow state. This confirms that the bridge voltage is generated by the flux flow resistance. In addition, the dynamic critical current of the HTS bridge slightly increases during the charging process (as shown in the insets of Fig. 11). According to Eq. (7), a small increase in the critical current can result in a noticeable difference in the induced voltage within the superconductor.

The losses in the HTS bridge and the separated loss contributions are shown in Fig. 12. The bridge losses decrease as a function of time owing to the reduction of the bridge voltage. Moreover, the loss contribution from the superconductor gradually becomes dominant. When the load current reaches its maximum (around 3 s), the total losses caused by the HTS bridge are estimated to be 3.54 J/m.

5.2. Characterization of secondary resistance

The secondary resistance connected in the charging loop has been proven to be crucial for achieving the optimum performance of the flux pump. Analytically, the reason has been clarified in terms of the magnetic flux coupling with the load loop and charging loop [27]. In this section, we will reveal its underlying mechanism from a circuit point of view. The secondary current and the corresponding secondary voltage as well as their net values are plotted in Fig. 13. The secondary voltage is defined as the voltage drop across the secondary resistance and can be calculated as, (see Fig. 14)

$$V_s(t) = \frac{\int_s E_j(t) ds}{S}. \quad (13)$$

The net current and the voltage first rise and then gradually reduce to zero. Referring to the circuit depicted in Fig. 1, the increase in secondary current and voltage can be attributed to the fact that the voltage generated by the bridge is applied to both ends of the load coil, and the secondary circuit is composed of the secondary winding and resistance. As a result, both the load current and secondary current increase in response to this voltage. This indicates that the secondary circuit is also being charged during the charging process. As the entire system is superconducting, the current generated in the charging loop would not be able to decay and would continuously circulate in the loop if the secondary resistance is not present. As a consequence, as demonstrated in a previous simulation by [48], this current will weaken the load current. This current can be eliminated in the presence of the secondary resistance, thereby increasing the load current. The process can be viewed as either the discharging of the charging loop or the charging of the load loop. Overall, the secondary circuit is first charged and then discharged during the charging process.

Given that the net value of the bridge voltage continuously decreases during the charging process, while the secondary voltage increases during the charging of the secondary circuit, we argue that once the secondary voltage equals the bridge voltage, the secondary circuit can no longer be charged and tends to be discharged. Furthermore, as previously discussed, the charging of the load coil is complete when the net value of the bridge voltage drops to zero, suggesting that the net value of the bridge voltage will eventually vanish. If the secondary voltage and the bridge voltage are not in agreement, the discharge of the secondary circuit will not stop. This means that all the

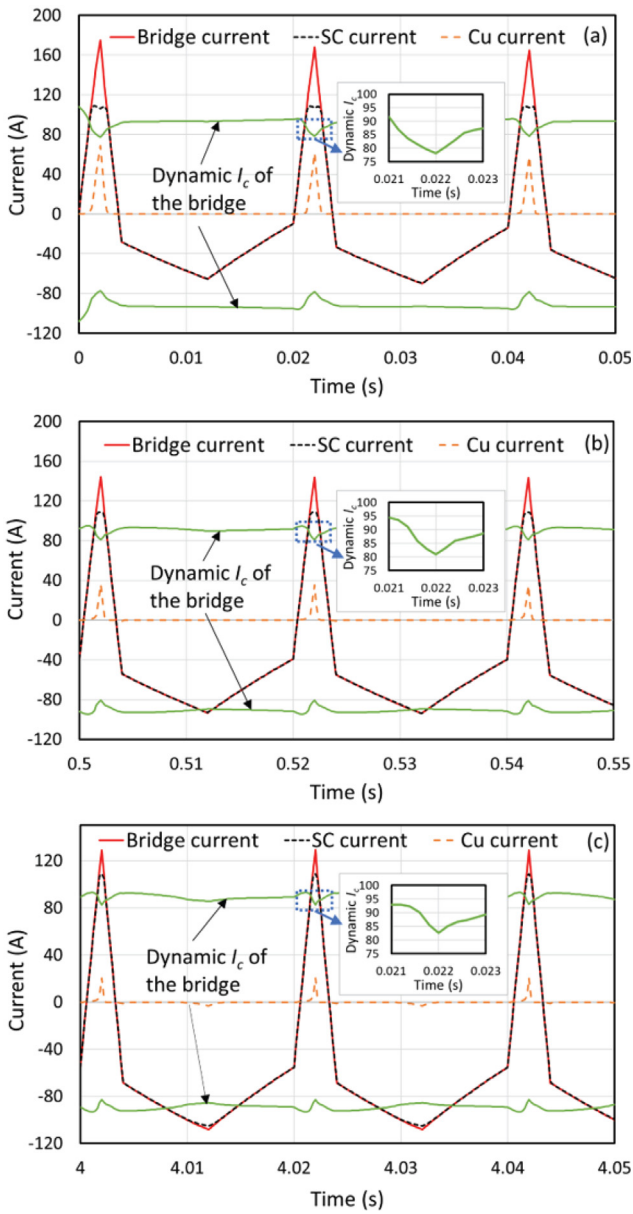


Fig. 11. Simulated current components within the HTS bridge as a function of time, at various charging stages including (a) the beginning, (b) when the load current rises, and (c) when the current reaches saturation. The insets illustrate the dynamic critical current of the bridge as the carrying current approaches the maximum value.

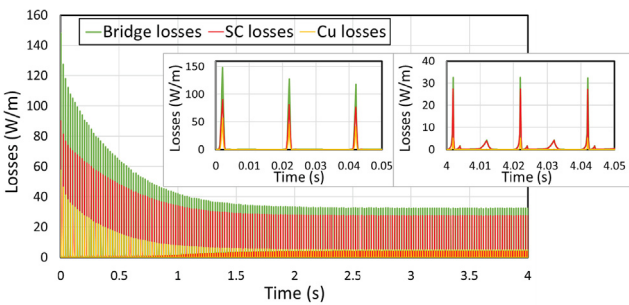


Fig. 12. Simulated bridge losses and the different loss components. The insets show the detail of the losses at the beginning and when the charging process is completed.

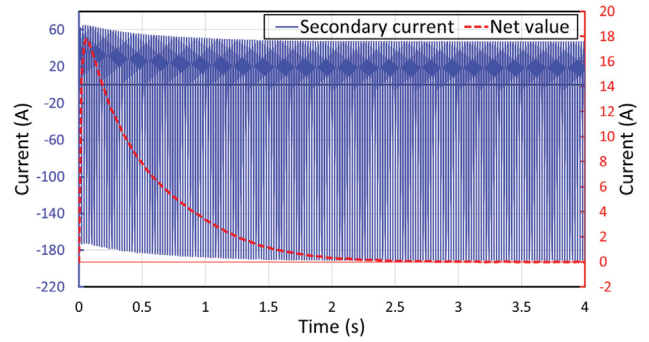


Fig. 13. Simulated secondary current and its net value over time.

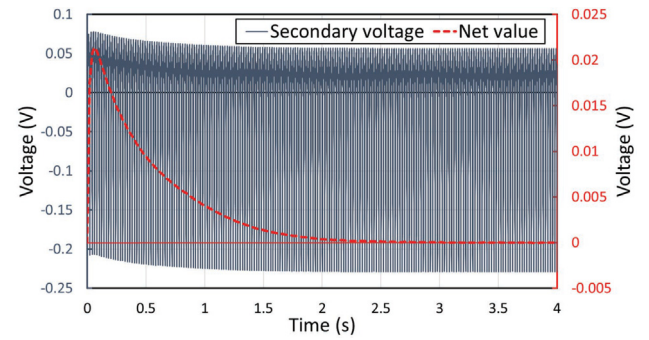


Fig. 14. Simulated secondary voltage and its net value over time.

current injected into the charging loop will completely decay. In Fig. 15, we show the net values of the secondary voltage and bridge voltage as a function of time to support our argument. The secondary voltage rises until it equals the bridge voltage, then starts to decline until it reaches zero.

According to the above analysis, the charging process is clear and can be summarized as follows: the voltage generated on the HTS bridge, the load coil and the secondary circuit are charged simultaneously; the secondary current continues to increase until the net voltage on the resistance reaches the net voltage on HTS bridge; then, the secondary current starts to decrease towards zero; at the same time, the net values of the secondary and bridge voltages decrease to zero and the load current reaches its maximum, which is equal to the reduction in bridge current.

Fig. 16 shows the secondary circuit losses, which include the hysteresis of the secondary winding and the secondary resistance losses, which are given by

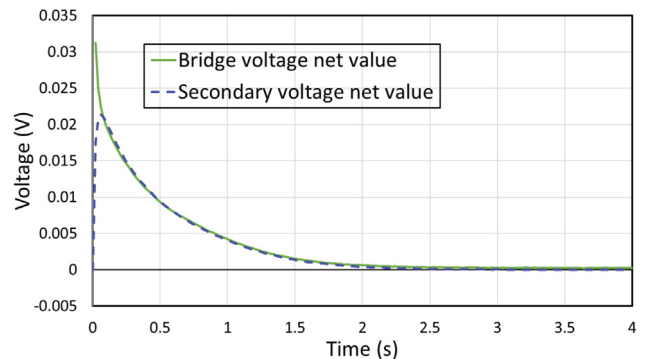


Fig. 15. Simulated net values of the bridge voltage and secondary voltage.

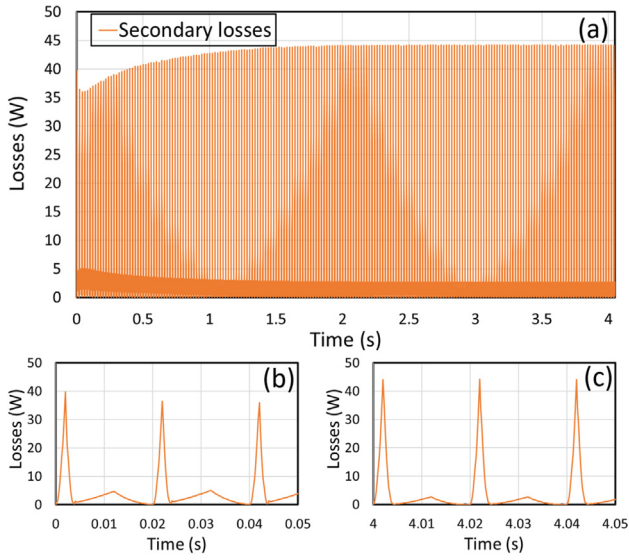


Fig. 16. Simulated secondary winding losses and secondary resistance losses for (a) the entire charging process, (b) the initial period of charging, and (c) the period after the charging process was completed.

$$Q_s = \int_s (E_z + E_j) \cdot J_z ds. \quad (14)$$

where Q_s is secondary circuit losses, E_z is electric field generated by the secondary winding, and E_j is electric field generated by the secondary resistances.

The losses vary with the variation of the secondary current and the total losses, as an integration of the losses over time, are estimated to be 11.54 J until the load current reaches its maximum.

5.3. Load current for different frequencies and secondary resistances

This section investigates the effect of applied frequency and secondary resistance on the charging performance. As shown in Fig. 17, regardless of the applied frequency, the general features revealed by the simulations are: i) for a secondary resistance of 0 Ω, or an extremely small value, the load current quickly reaches saturation at a significantly lower value than when a non-zero secondary resistance is present; ii) with the secondary resistance, the charging performance is improved, and the saturation load current can be maximized. Additionally, increasing the secondary resistance results in faster charging speeds; iii) beyond a certain point, further resistance increase results in a reduction in saturation load current. The transition value of the secondary resistance depends on the frequency and increases with the applied frequency. For feature i), it is because the secondary current generated by the charging loop cannot be removed. Fig. 18 presents the waveform and the net value of the secondary current for a secondary resistance of 0 Ω. As previously stated, the current first ramps up, and then keeps circulating in the charging loop without any decay (or a negligible decay). In this scenario, the saturation value of the load current is determined by the current flowing into the charging loop, which is dependent on the impedance ratio between the charging loop and the load loop. For feature ii), as concluded in Section 5.2, all current generated in the charging loop will fully decay due to the secondary resistance by the end of the charging process. In addition, higher resistance results in a smaller time constant (Eq. 15), resulting in faster charging and discharging in the secondary circuit, and therefore shortening the overall charging time. The time constant is given as,

$$\tau = L_s/R_j \quad (15)$$

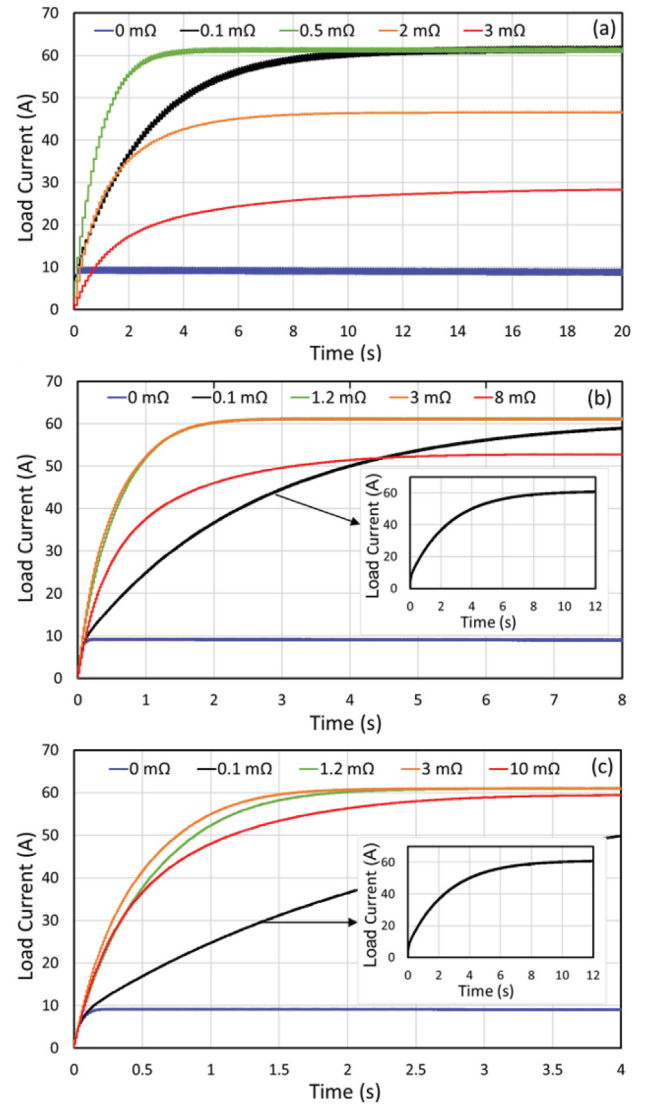


Fig. 17. Simulated load current for different secondary resistances at varying frequencies: (a) 10 Hz, (b) 50 Hz, and (c) 100 Hz.

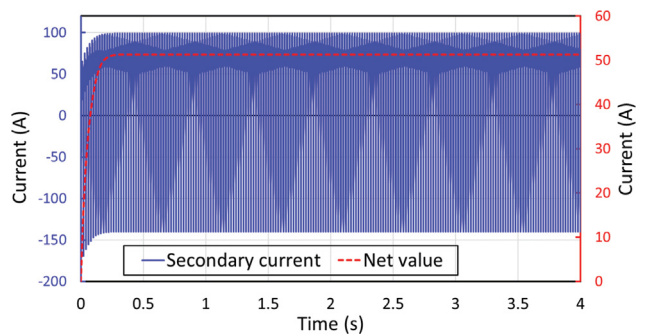


Fig. 18. Simulated secondary current for a secondary resistance of 0 Ω and applied frequency of 50 Hz.

where L_s is the secondary inductance, and R_j is the secondary resistance.

To prove this, the bridge voltages and the secondary voltages for secondary resistances of 0.1 mΩ and 1.2 mΩ at an applied frequency of 50 Hz are plotted in Fig. 19. It is clear that with for a higher sec-

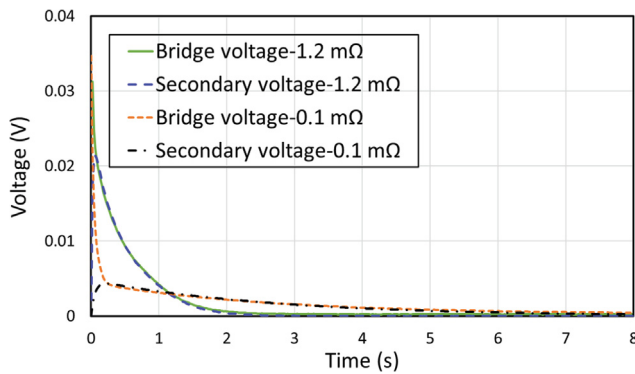


Fig. 19. The curve of the load coil current charged with the flux pump using two different secondary resistances: 1.2 m Ω and 0.1 m Ω .

ondary resistance, the bridge voltage drops to zero in a shorter period. The last feature is due to the secondary current being incapable of tracking the primary current (see Fig. 20), which is caused by the large load impedance [12]. In order to maintain tracking between the primary and secondary currents, the threshold for the secondary resistance increases as the applied frequency increases. The above-mentioned observations are different in many ways from the experimental results reported by [27,6]. When a smaller secondary resistance is used in these experiments, the charging speed is slower than predicted, but the load current decreases. A possible reason is that the measurement time is not long enough, so the load current did not reach its maximum value. For example, [27], discovered that with a secondary resistance of 0.5 m Ω , the load current was still increasing at the end of the experiment. As shown in our study, the difference in the charging time can be one order of magnitude.

In addition, in Fig. 21, we found that the load current waveforms for the same secondary resistance at different frequencies almost coincide. Except for the case of a secondary resistance of 1.2 m Ω , the charging speed and the saturation current are lower at 10 Hz due to the relatively larger impedance. According to Eq. (12), and as we discussed in Section 5.1, the bridge voltage V_L is mainly determined by the flux flow resistance of the superconductor, which is frequency independent. Additionally, the net voltage applied on the load coil is independent of the applied frequency. The charging performance is thus frequency independent. This behavior is undoubtedly due to the fact that maintaining tracking between the primary and secondary currents, namely, the load impedance, is restricted to a certain level.

The preceding observation suggests that, given the evidence that load resistance would not affect the magnitude of the secondary current, the optimum charging performance is achieved by using a high-enough secondary resistance. In terms of losses, high resistance

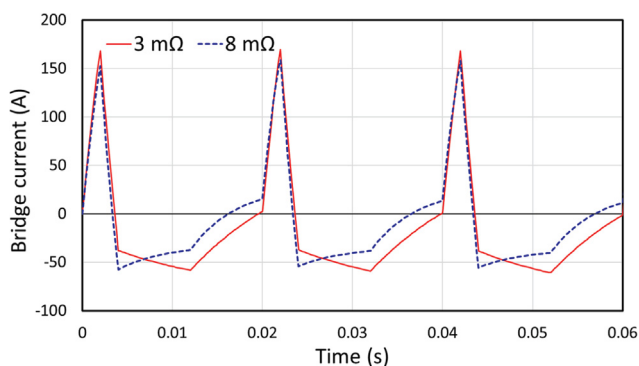


Fig. 20. The bridge current for different secondary resistances (3 m Ω and 8 m Ω) for an applied frequency of 50 Hz.

normally results in large losses in the unit period and may result in higher total losses, even though it can shorten the operation time. Therefore, the selection of the most appropriate secondary resistance must be thoroughly investigated. For instance at an applied frequency of 50 Hz: i) for the secondary resistance of 0.1 m Ω , which takes about 12 s to complete the charging process, the total losses the bridge and due to the secondary circuit are estimated to be 11.96 J/m and 4.65 J, respectively; ii) for the secondary resistance of 1.2 m Ω , which takes about 3 s to complete the charging process, the total losses are estimated to be 3.54 J/m and 11.25 J, respectively; iii) and for the secondary resistance of 3 m Ω , which takes about 3 s to complete the charging process, the total losses are estimated to be 3.14 J/m and 26.9 J, respectively. After thoroughly evaluating the charging performance and total losses, it was determined that the most appropriate value of load resistance for the current study is 1.2 m Ω .

6. Conclusion

An electrical contact-free injection of direct current into a closed superconducting circuit is achieved by the self-regulating HTS flux pump. The use of numerical prediction tools is essential to ensure comprehensive system design, optimization, and successful implementation. A 2D H-formulation FEM model was created and coupled with an electrical circuit to thoroughly investigate the charging process of a coil utilizing the self-regulating HTS flux pump. To explore the impact of secondary resistance on the charging performance of the flux pumps, an additional electrical component was incorporated into the governing equation within the 2D H-formulation FEM model. At the same time, the losses caused by superconducting elements are also assessed. The simulation results revealed that by applying an asymmetric current with a positive magnitude greater than the critical current of the HTS bridge, the parallel-connected coil can be charged gradually through the net voltage produced by the bridge. The accuracy of the method is demonstrated by comparing the calculated bridge voltage to its experimentally-measured value. The good agreement suggests that the induced flux flow resistance is the primary cause of the net voltage generated by the HTS bridge.

The working principle and underlying mechanism of the secondary resistance operation are illustrated using this model. Specifically, a non-removable induced direct current circulates in the charging loop due to the negligible secondary resistance. This current reduces the maximum value that the load current can achieve, and the added secondary resistance can consume this induced current, improving the charging performance. More importantly, we found that this resistance can eliminate the undesirable direct current. This means that when the current applied to the bridge is of the same magnitude, the load current eventually reaches the same maximum saturation value under different secondary resistances. Additionally, given this premise, using a higher secondary resistance can accelerate the charging process due to a lower time constant, but it will also generate more losses. Therefore, it is crucial to thoroughly investigate the secondary resistance, taking into account variables like the saturation load current, charging speed, and generated losses, to achieve optimal charging performance. Finally, the numerical method presented here shows promising performance in describing the charging process of a coil using the self-regulating HTS flux pump. It effectively captures all the essential characteristics and proves to be reliable for designing and optimizing this type of flux pump, thereby accelerating its practical application.

Declaration of Competing Interest

The authors declared that there is no conflict of interest.

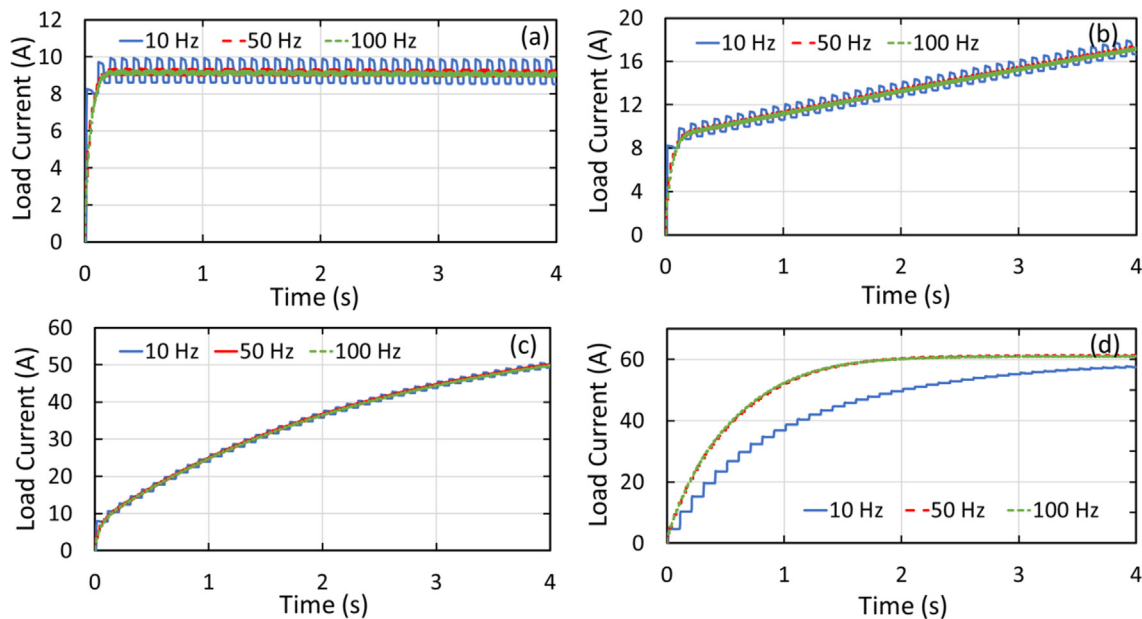


Fig. 21. Simulated load current under different frequencies (10, 50 and 100 Hz) for secondary resistances of (a) 0 mΩ, (b) 0.01 mΩ, (c) 0.1 mΩ, and (d) 1.2 mΩ.

References

- [1] Ainslie MD, Bumby CW, Jiang Z, Toyomoto R, Amemiya N. Numerical modelling of dynamic resistance in high-temperature superconducting coated-conductor wires. *Supercond Sci Technol* 2018;31:074003.
- [2] Brooks J, Ainslie M, Jiang Z, Pantoja A, Badcock R, Bumby C. The transient voltage response of rebco coated conductors exhibiting dynamic resistance. *Supercond Sci Technol* 2020;33:035007.
- [3] Bumby C, Jiang Z, Storey J, Pantoja A, Badcock R. Anomalous open-circuit voltage from a high- T_c superconducting dynamo. *Appl Phys Lett* 2016;108. Art. no. 122601.
- [4] Bumby CW, Pantoja AE, Sung HJ, Jiang Z, Kulkarni R, Badcock RA. Through-wall excitation of a magnet coil by an external-rotor HTS flux pump. *IEEE Trans Appl Supercond* 2016;26:1–5.
- [5] Coombs T. Superconducting flux pumps. *J Appl Phys* 2019;125:230902.
- [6] Deng Y, Li J, Zhou P, Sun C, Zhai Y, Qian H, et al. Performance optimization and verification of the transformer-rectifier flux pump for HTS magnet charging. *IEEE Trans Appl Supercond* 2020;30:1–5.
- [7] Dos Santos G, Martins F, Sassi F, Dias D, Sotelo G, Morandi A. A coupling method of the superconducting devices modeled by finite element method with the lumped parameters electrical circuit. *Supercond Sci Technol* 2021;34:045014.
- [8] Fu L, Matsuda K, Baghdadi M, Coombs T. Linear flux pump device applied to high temperature superconducting (HTS) magnets. *IEEE Trans Appl Supercond* 2015;25:1–4.
- [9] Fu W, Zhao Y, Ho SL, Zhou P. An electromagnetic field and electric circuit coupled method for solid conductors in 3-d finite-element method. *IEEE Trans Magn* 2015;52:1–4.
- [10] Geng J, Bumby CW, Badcock RA. Maximising the current output from a self-switching ka-class rectifier flux pump. *Supercond Sci Technol* 2020;33:045005.
- [11] Geng J, Coombs T. Mechanism of a high- T_c superconducting flux pump: Using alternating magnetic field to trigger flux flow. *Appl Phys Lett* 2015;107:142601.
- [12] Geng J, Coombs T. An HTS flux pump operated by directly driving a superconductor into flux flow region in the E-J curve. *Supercond Sci Technol* 2016;29:095004.
- [13] Geng J, Coombs TA. Modeling methodology for a HTS flux pump using a 2D H-formulation. *Supercond Sci Technol* 2018;31:125015.
- [14] Geng J, Li C, Coombs TA. A fast ac field controlled impedance in hts coated conductors: Response speed and electric field value. *IEEE Trans Appl Supercond* 2017;27:1–5. <https://doi.org/10.1109/TASC.2017.2716834>.
- [15] Geng J, Matsuda K, Fu L, Fagnard JF, Zhang H, Zhang X, et al. Origin of dc voltage in type II superconducting flux pumps: field, field rate of change, and current density dependence of resistivity. *J Phys D: Appl Phys* 2016;49. Art. no. 11LT01.
- [16] Ghabeli A, Ainslie M, Pardo E, Quéval L, Mataira R. Modeling the charging process of a coil by an HTS dynamo-type flux pump. *Supercond Sci Technol* 2021;34:084002.
- [17] Hoffmann C, Pooke D, Caplin AD. Flux pump for HTS magnets. *IEEE Trans Appl Supercond* 2010;21:1628–31.
- [18] Iftikhar MH, Geng J, Yuan W, Zhang M. A noninductive bifilar coil to design compact flux pumps for HTS magnets. *IEEE Trans Appl Supercond* 2022;32:1–7.
- [19] Jiang Z, Hamilton K, Amemiya N, Badcock R, Bumby C. Dynamic resistance of a high- T_c superconducting flux pump. *Appl Phys Lett* 2014;105:112601.
- [20] Jin JX, Zheng LH, Guo YG, Zhu JG, Grantham C, Sorrell CC, Xu W. High-temperature superconducting linear synchronous motors integrated with hts magnetic levitation components. *IEEE Trans Appl Supercond* 2012;22. 5202617–5202617.
- [21] Kaneko Y, Kitamura T, Nakamura K, Takao T. Corrections to levitation force improvement by effective magnetic interaction in two magnetic levitation systems with hts coil and bulks. *IEEE Trans Appl Supercond* 2020;30. 1–1.
- [22] Kaneko Y, Kitamura T, Nakamura K, Takao T. Levitation force improvement by effective magnetic interaction in two magnetic levitation systems with hts coil and bulks. *IEEE Trans Appl Supercond* 2020;30:1–6.
- [23] Kim JH, Park SI, Kim HM. Magnetic field analysis of the field coil for 10 mw class superconducting wind turbines. *Progress Supercond Cryogen (PSC)/J Korea Inst Appl Supercond Cryogen* 2012;14.
- [24] Van de Klundert L, ten Kate HH. Fully superconducting rectifiers and fluxpumps part 1: Realized methods for pumping flux. *Cryogenics* 1981;21:195–206.
- [25] Leclerc J, Masson PJ. Testing of a subscale hts coil for wind turbine generator. *IEEE Trans Appl Supercond* 2016;26:1–4.
- [26] Leuw B, Geng J, Rice JH, Moseley DA, Badcock RA. A half-wave superconducting transformer-rectifier flux pump using $J_c(B)$ switches. *Supercond Sci Technol* 2022;35:035009.
- [27] Li C, Geng J, Shen B, Ma J, Gawith J, Coombs TA. Investigation on the transformer-rectifier flux pump for high field magnets. *IEEE Trans Appl Supercond* 2019;29:1–5.
- [28] Li C, Yang J, Shen B, Ma J, Gawith J, Öztürk Y, et al. A HTS flux pump simulation methodology based on the electrical circuit. *IEEE Trans Appl Supercond* 2020;30:1–5.
- [29] Li J, Sun C, Zhou P, Li S, Wang R, Ren G, et al. Influence of ferromagnetic slice on the charging performance of a through-wall HTS flux pump employing a magnetic coupler. *Supercond Sci Technol* 2022;35:075008.
- [30] Ma J, Geng J, Coombs T. Flux pumping for non-insulated and metal-insulated hts coils. *Supercond Sci Technol* 2017;31:015018.
- [31] Mataira R, Ainslie M, Badcock R, Bumby C. Origin of the DC output voltage from a high- T_c superconducting dynamo. *Appl Phys Lett* 2019;114. Art. no. 162601.
- [32] Mataira R, Ainslie M, Pantoja A, Badcock R, Bumby C. Mechanism of the high- T_c superconducting dynamo: Models and experiment. *Phys Rev Appl* 2020;14:024012.
- [33] Ostrenko M, Andriienko B. Transformer impulse surges calculation by fem coupled to circuit. *IEEE Trans Magn* 2017;53:1–4.
- [34] Qian C, Masad IS, Rosenberg JT, Elumalai M, Brey WW, Grant SC, et al. A volume birdcage coil with an adjustable sliding tuner ring for neuroimaging in high field vertical magnets: Ex and in vivo applications at 21.1 t. *J Magn Reson* 2012;221.
- [35] Senatore C, Alessandrini M, Lucarelli A, Tediosi R, Uglietti D, Iwasa Y. Progresses and challenges in the development of high-field solenoidal magnets based on re123 coated conductors. *Supercond Sci Technol* 2014;27:103001.
- [36] Sharma DK, Bathula V, Gour AS, Rao VV. Investigation on effect of shape of hts pole coil on airgap magnetic field of hts synchronous motor. *IOP Publishing Ltd.*; 2022.
- [37] Shen B, Grilli F, Coombs T. Overview of H-formulation: A versatile tool for modeling electromagnetics in high-temperature superconductor applications. *IEEE Access* 2020;8:100403–14.

- [38] Storey JG, Pantoja AE, Jiang Z, Badcock RA, Bumby CW. Optimizing rotor speed and geometry for an externally mounted HTS dynamo. *IEEE Trans Appl Supercond* 2019;29:1–5.
- [39] Sung HJ, Badcock RA, Go B, Park M, Yu I, Jiang Z. Design of a 12-MW HTS wind power generator including a flux pump exciter. *IEEE Trans Appl Supercond* 2016;26:1–5.
- [40] Wang W, Wei J, Yang C, Wu C, Li H. Review of high temperature superconducting flux pumps. *Superconductivity* 2022;100022.
- [41] Weijers H, Trociewitz U, Markiewicz W, Jiang J, Myers D, Hellstrom E, et al. High field magnets with hts conductors. *IEEE Trans Appl Supercond* 2010;20:576–82.
- [42] Wen Z, Zhang H, Mueller M. High temperature superconducting flux pumps for contactless energization. *Crystals* 2022;12:766.
- [43] Yamasaki H, Natori N, Furuse M. Evaluation of heat leak in a model superconducting coil module for a wind turbine generator with iron cores. *IEEE Trans Appl Supercond* 2015;25:1–5.
- [44] Zermeno V, Krüger P, Takayasu M, Grilli F. Modeling and simulation of termination resistances in superconducting cables. *Supercond Sci Technol* 2014;27:124013.
- [45] Zhai Y, Ma G, Deng Y, Sun C, Li Y, Zhou P. Modeling and characteristics investigation of self-regulating HTS flux pump. *Cryogenics* 2022;103486.
- [46] Zhai Y, Zhou P, Li J, Sun C, Li Y, Xiao L, et al. Performance investigation of contactless self-regulating HTS flux pump. *IEEE Trans Appl Supercond* 2021;31:1–5.
- [47] Zhou P, Dos Santos G, Ghabeli A, Grilli F, Ma G. Coupling electromagnetic numerical models of hts coils to electrical circuits: multi-scale and homogeneous methodologies using the ta formulation. *Supercond Sci Technol* 2022;35:115005.
- [48] Zhou P, Ma G, Deng Y, Nie X, Zhai Y, Liu K, et al. A contactless self-regulating HTS flux pump. *IEEE Trans Appl Supercond* 2020;30:1–6.
- [49] Zhou P, Ma G, Quéval L. Transition frequency of transport ac losses in high temperature superconducting coated conductors. *J Appl Phys* 2019;126:063901.
- [50] Zhou P, Wang C, Qian H, Queval L, Luo Z, Deng Y, et al. Frequency-dependent transport ac losses of coated superconductors up to tens of kilohertz. *IEEE Trans Appl Supercond* 2019;29:1–5.